Orthogonal micro-organization of orientation and spatial frequency in primate primary visual cortex

Ian Nauhaus[1,2], Kristina J Nielsen[1,2], Anita A Disney[1] & Edward M Callaway[1]

Orientation and spatial frequency tuning are highly salient properties of neurons in primary visual cortex (V1). The combined organization of these particular tuning properties in the cortical space will strongly shape the V1 population response to different visual inputs, yet it is poorly understood. In this study, we used two-photon imaging in macaque monkey V1 to demonstrate the three-dimensional cell-by-cell layout of both spatial frequency and orientation tuning. We first found that spatial frequency tuning was organized into highly structured maps that remained consistent across the depth of layer II/III, similarly to orientation tuning. Next, we found that orientation and spatial frequency maps were intimately related at the fine spatial scale observed with two-photon imaging. Not only did the map gradients tend notably toward orthogonality, but they also co-varied negatively from cell to cell at the spatial scale of cortical columns.

It has been about 50 years since Hubel and Wiesel's seminal experiments demonstrating an orderly, columnar representation of orientation and ocular dominance preference across primary visual cortex[1,2]. Since then, optical imaging experiments have explicitly shown the two-dimensional layouts of these maps with their characteristic orientation 'pinwheels' and ocular dominance 'bands'[3,4]. Although it is unknown whether the existence of orderly functional maps benefits cortical processing[5], their layout and alignment are likely to put constraints on the ability of V1 to represent all stimulus features for each eye and at each region of visual space. Early on, it was suggested that the tiling of feature space in V1 is optimized to overcome this constraint[6]. Indeed, optical imaging has demonstrated that orientation pinwheels align with ocular dominance bands[7–9] and that the cortical magnification factor is lower along the axis of the ocular dominance bands[10]. Both relationships are consistent with an architecture that is optimized for uniform coverage and are perhaps the clearest demonstration of how multiple stimulus features are jointly encoded in V1. Spatial frequency is another important stimulus feature encoded in V1, yet the functional architecture of spatial frequency tuning is less clear than that of orientation tuning or ocular dominance. Most of the studies that mapped orientation and spatial frequency preference in cats or ferrets concluded that the maps are systematically related[11–13], but others reported otherwise[14,15]. Evidence on this topic in macaque V1 is much scarcer. Furthermore, the architecture of cat and ferret visual cortex is markedly different from that of primate V1, indicating that interactions between feature representations may not be universal.

Although previous studies have presented evidence for some degree of spatial frequency clustering in macaque monkey V1, the architecture of spatial frequency tuning is essentially unknown. For instance, spatial frequency tuning is often similar between nearby cells measured with extracellular electrodes[16–18], although the similarity is less pronounced than that for orientation[2], and there is disagreement on the degree of continuity. Similarly, a study using 2-[^{14}C]deoxyglucose (2DG) uptake showed that gratings of high or low spatial frequency yield patchy activation patterns[19]. Available evidence on the combined organization of spatial frequency tuning with other feature maps is even weaker, although orderly relationships seem plausible when previous observations are considered: neurons that prefer lower spatial frequency tend to cluster near the cytochrome oxidase 'blobs'[16–19], blobs lie at the center of ocular dominance bands[20], and ocular dominance maps are orthogonal to orientation maps[7,8]. Taken together, this suggests a systematic relationship between orientation and spatial frequency maps, which is of particular interest with regard to the ability of V1 to efficiently represent visual space. On the basis of the observation that spatial frequency tuning is clustered less than orientation tuning, it seems likely that methodological limitations have prevented a clear picture of these relationships from emerging: intrinsic signal imaging, for example, lacks single-cell resolution, and single-unit recordings lack sufficient sampling density. To fully address how orientation and spatial frequency are jointly represented, it is necessary to measure their organization with single-cell resolution.

Here, building on previous studies using two-photon imaging of a bulk loaded calcium indicator[21] to investigate functional micro-architecture in visual cortex[22], we characterized orientation and spatial frequency tuning in layer II/III of macaque monkey V1. We found that two-photon calcium imaging allowed high-density sampling from large populations of macaque V1 neurons, yielding significant responses from about 94% of neurons. We quantified the degree of clustering for both parameters, on the basis of cell pairings at different cortical distances. The normalized degree of clustering was higher for orientation than spatial frequency tuning; however, both showed significant clustering. The substantial clustering of orientation tuning is a reflection of its organization into precise compartments with

Figure 1 Two experimental two-photon imaging procedures. (**a**–**d**) Large-scale imaging. (**a**) We used a 16× objective lens (~3 µm pixel⁻¹) and drifting gratings to measure orientation and spatial frequency tuning curves at each pixel (scale bar, 500 µm). (**b**) Mean and s.e.m. time course for each combination of orientation and spatial frequency for the pixel circled in red in **a**. Shown are the time courses for the best (blue) and worst (red) combinations. The thin black line represents the stimulus presentation period. (**c**,**d**) Orientation and spatial frequency tuning curves computed by taking the mean within the stimulus presentation period. (**c**) Orientation tuning for the pixel outlined in red in **a**. (**d**) Spatial frequency tuning curve for the same pixel. (**e**–**h**) Fine-scale imaging (scale bar, 50 µm). (**e**) To measure responses of individual neurons, we imaged with higher resolution (~0.8 µm pixel⁻¹). Instead of drifting gratings, this paradigm used flashed gratings shown in rapid succession. (**f**) The average transient response to two gratings within our randomized flashed grating stimulus for the neuron circled in **e**. (**g**,**h**) Raw orientation tuning and spatial frequency tuning curves (black dots) and fits (red line).
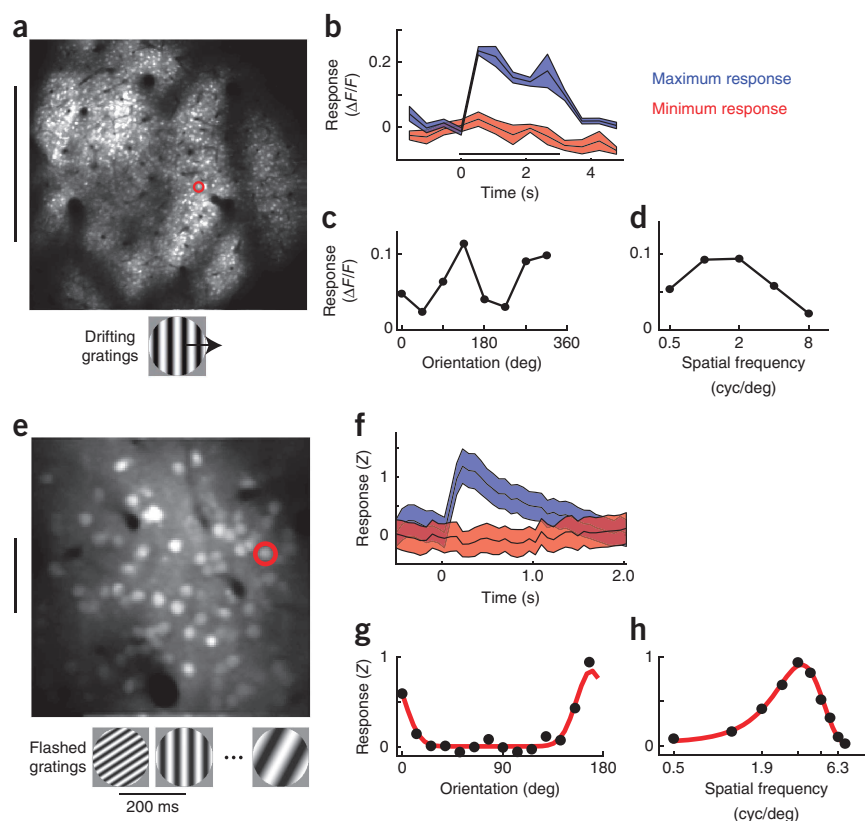
well-defined borders, consistent with previous findings in the cat[22]. As also suggested by the clustering metric, spatial frequency preference was organized into highly structured maps that were consistent across the depth of layer II/III. Finally, we found that the orientation and spatial frequency maps were organized with respect to each other in a systematic fashion: their smoothed contours ran orthogonally to each other. Consistently, we also found that the joint distribution of their gradient magnitudes was significantly anticorrelated at the finest spatial scale.

RESULTS

We imaged visual responses in layer II/III of monkey V1 using two-photon imaging with the calcium indicator Oregon Green BAPTA-1 AM (OGB-1). Imaging was performed at two spatial scales, which we refer to as 'large-scale' and 'fine-scale' imaging (**Fig. 1**). To achieve large-scale imaging, we made several adjacent OGB-1 injections and imaged a V1 region of about 800 × 800 µm at a resolution of ~3 µm pixel⁻¹ with a 16× objective lens (**Fig. 1a**). Tuning curves were computed on a per-pixel rather than a per-cell basis because the lower resolution made it difficult to separate the responses of cell bodies from that of the background neuropil. However, the large field of view results in a more global representation of the maps. For fine-scale imaging, we zoomed in on the maps, imaging a region of about 200 × 200 µm (~0.8 µm pixel⁻¹) with a 40× objective to capture the cell-by-cell tuning organization (**Fig. 1e**). In this case, tuning curves were computed for each cell individually. We used different stimuli to measure orientation and spatial frequency tuning at the two imaging resolutions. For the large-scale imaging, we showed drifting gratings and quantified stimulus preferences as the center of mass of the tuning curves (**Fig. 1c,d**). For the fine-scale imaging, we showed a sequence of rapidly flashed gratings[23] and calculated the expected response transient to each combination of orientation and spatial frequency, followed by subtracting the expected response to an interleaved blank. The dynamics of the transient shown in **Figure 1f** are typical. Across our population of neurons, the average time-to-peak of the raw

response to the best grating was 278 (± 72 s.d.) ms and the average full-width at half-maximum was 479 (± 237 s.d.) ms. Tuning curves were taken at the time-to-peak and fit with a function to characterize their shape (**Fig. 1g,h**). We have previously shown advantages of using a randomized noise stimulus over drifting gratings to recover accurate tuning curves with calcium imaging[24]. Additionally, we found here that about 94% of the imaged neurons yielded reliable responses to the visual stimulus and that tuning curves could be well parameterized from about 93% of the remaining responsive neurons. A summary of the tuning parameters from this population is given in **Supplementary Figure 1**. Two-photon imaging in the monkey thus has advantages over other recording techniques in terms of its ability to measure neuronal tuning from a dense sampling of neurons in a specified anatomical location.

Orientation and spatial frequency maps in layer II/III

Large-scale imaging of V1 revealed a highly structured map of spatial frequency in V1, in addition to the well-known orderly representation of orientation (**Fig. 2**). As expected, the orientation maps exhibited a pinwheel structure that was consistent at both depths (**Fig. 2a,b,e,f**). Unlike orientation tuning, the layout of spatial frequency preference across V1 has been unclear. Our data demonstrate substantial structure in preferred spatial frequency—low or high spatial frequency preference is clustered with smooth transitions in between—and that this structure is consistent across the two depths tested here.

To compare the degree of consistency across the depth of layer II/III between the orientation and spatial frequency maps, we computed a normalized metric for map similarity at the two imaging depths. The absolute difference in preferred orientation and spatial frequency between the maps at the two depths was taken for each pixel and then averaged across pixels. To normalize, this mean difference was then recomputed after random resampling of the two maps at

Figure 2 Large-scale imaging of orientation and spatial frequency maps at different depths of layer II/III for two cortical locations. (**a,b**) Orientation preference maps at cortical depths of 210 μm and 310 μm. (**c,d**) Spatial frequency maps obtained from the same experiment. Both orientation and spatial frequency maps maintain a very similar structure across the two depths. Dark map regions indicate portions of the map with low SNR (see Online Methods). (**e–h**) A second cortical region at two depths: 180 μm and 280 μm. Scale bar, 0.5 mm (**a–h**).

independent locations. On the basis of this metric, the orientation maps at the two depths were about three times more similar than the spatial frequency maps for both imaging regions (**Fig. 2**). These differences were significant ($P < 0.01$; bootstrap).

Cell-by-cell clustering of orientation and spatial frequency tuning
Having established an orderly representation of spatial frequency preference across V1 on a more global scale, we next studied the layout of spatial frequency preference at a finer resolution (**Fig. 3**). The fine-scale imaging mode allowed us to determine orientation and spatial frequency tuning on a cell-by-cell basis ('micro-maps'). Depth of imaging ranged from ~150 μm to ~250 μm for these maps. As previously shown in cat V1 with two-photon imaging[22], our data confirmed that orientation tuning is highly organized in the primate (**Fig. 3a**). Consistent with the results of our large-scale imaging experiments, spatial frequency preference also progressed continuously over the localized patch of neurons (**Fig. 3b**). However, spatial frequency maps seemed to exhibit more scatter than the orientation maps.

We quantified how strongly orientation and spatial frequency preference were clustered across neurons by computing a clustering metric, $C(d)$. This metric takes the expected tuning similarity between cell pairings separated by a given cortical distance d (**Fig. 4a,b**) and then normalizes by the local map statistics computed by random resampling. $C(d) > 1$ or $C(d) < 1$ indicates that two cells separated by d microns are likely to have tuning more similar or different than the average resampled pair, respectively. Resampling was performed two ways. In the first case, randomly selected cell pairs came from the same imaging region, which captured the extent of clustering within imaging regions (~200 × 200 μm). In the second case, the two neurons in each pair could be from different imaging regions, thus measuring the extent of clustering relative to the entire population of imaged neurons in our data set. The analyses are based on all 735 neurons and all ~30,000 neuron pairs in ten imaging regions.

Computing the degree of clustering relative to the distribution of orientation and spatial frequency tuning in each imaging region revealed that $C(d)$ was >1 for distances less than ~100 μm and <1 for the larger distances (**Fig. 4c**). The gradual decline of $C(d)$ with distance reflects the map continuity that exists within these small imaging regions (~200 μm). Although the general trend of $C(d)$ was similar for orientation and spatial frequency maps, spatial frequency maps showed more scatter relative to the local map trend.

Figure 4d summarizes the degree of clustering relative to the overall distribution of orientation and spatial frequency tuning across all imaging regions. Under the assumption that our ten imaging regions represent an unbiased sample of orientation and spatial frequency tuning, this is the clustering relative to the distribution of orientation and spatial frequency tuning curves in layer II/III of parafoveal V1. The spatial decay of $C(d)$ reflects the spatial scale and periodicity of the maps (for example, at larger distances $C(d)$ may have another peak, and it will ultimately decay to 1). Although $C(d)$ decayed at a similar rate for orientation and spatial frequency, $C(d)$ for orientation was scaled higher, indicating that the orientation map was more continuous.
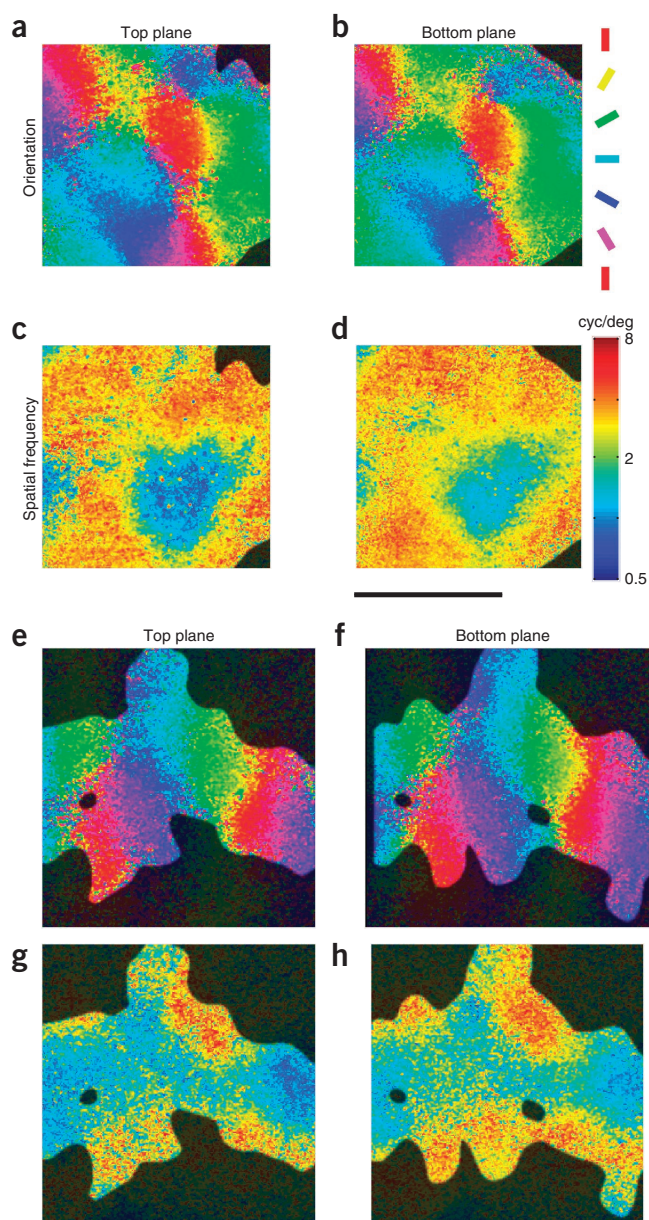
$C(d)$ was computed using the correlation coefficient between pairs of tuning curves. The averages of these correlation coefficients within each bin of cortical distance (**Fig. 4c,d**) for orientation were 0.88, 0.76, 0.64, 0.50 and 0.25 and for spatial frequency were 0.84, 0.76, 0.69, 0.64 and 0.57. Unlike $C(d)$, there was a tendency for the correlations to be higher for spatial frequency than orientation, which is most likely due to the sharper tuning of orientation than spatial frequency relative to the range of available peak locations.

Intersection of orientation and spatial frequency maps
As our data demonstrated that orientation and spatial frequency preference were both organized in a continuous fashion across V1, the question arose how the two maps are aligned with respect to each other. We first used data obtained from the large-scale imaging experiments to characterize how orientation and spatial frequency maps intersect. **Figure 5** shows the orientation and spatial frequency maps obtained from an imaging depth that is half the distance between the imaging planes shown in **Figure 2**. Before computing contours
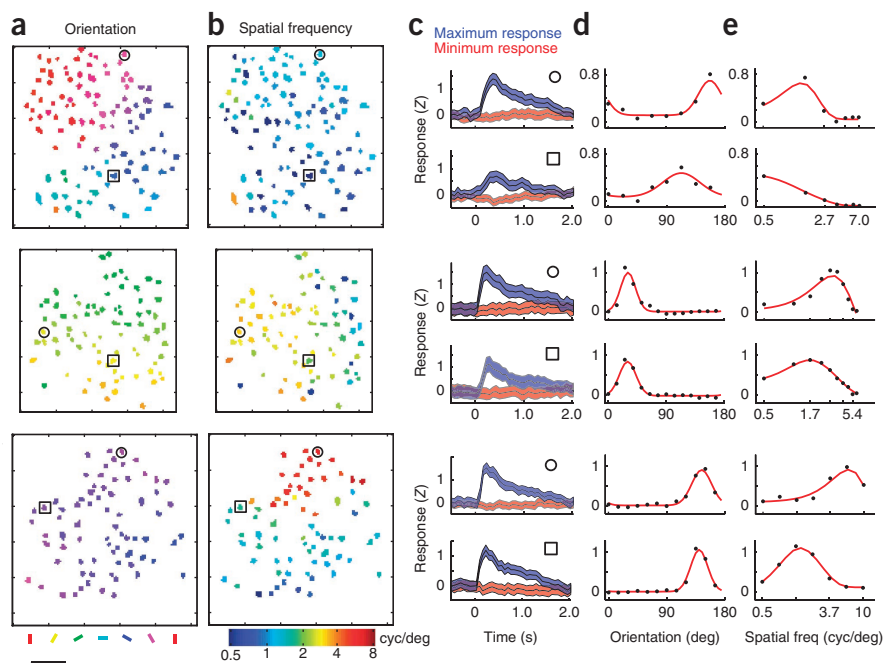
Figure 3 Micro-maps of orientation and spatial frequency for three example regions (one per row), each ~150 μm deep. (**a**,**b**) Each neuron's preference for orientation (**a**) and spatial frequency (**b**), color-coded. (**c**–**e**) For each region shown, average responses for two example neurons (circle and square). (**c**) Mean and s.e.m. response time course to the 'best' (blue) and 'worst' (red) combination of orientation and spatial frequency. Orientation (**d**) and spatial frequency (**e**) tuning curves (black dots) were computed at the optimal time delay and fit with Gaussian and difference-of-Gaussians function (red curve), respectively. Scale bar, 50 μm.

and gradients, we smoothed the raw data with a two-dimensional Gaussian (σ = 25 μm). Smoothing allowed us to capture the local trend of the gradients on the spatial scale of the smoothing operator. The contours of the orientation and spatial frequency maps appear to intersect orthogonally (**Fig. 5c,h**). To quantify the preferred angle of intersection, we first took the difference in the phase of the two map gradients at each pixel and binned these differences into a histogram (**Fig. 5d,i**). Indeed, the intersection histogram for each ROI showed peaks around ± 90°. The preferred intersection angle of the gradients was then computed as a function of the intersection histogram:

$$\text{Preferred intersection angle} = \text{angle}\left(\sqrt{\sum_\alpha H(\alpha)e^{i2\alpha}}\right)$$

where $H(\alpha)$ is the histogram value as a function of the intersection angle. Note that α is a direction (0° to 360°) and the preferred intersection angle is an orientation (0° to 180°). The preferred intersection angles for the two imaging regions in **Figure 5** were 94° and 84°. **Supplementary Figure 2** also shows three imaging

regions from two more animals that had preferred intersection angles of 95°, 79° and 99°. A Rayleigh test showed that $H(\alpha)$ was significantly different from uniform for all regions ($P < 10^{-100}$).

To compare the spatial scale of the orientation and spatial frequency maps, we computed their autocorrelation as a function of absolute cortical distance. For spatial frequency, we used the Pearson correlation coefficient at each shift to compute the autocorrelation. Because orientation is a circular variable, we chose to compute the autocorrelation function of the orientation map using a coherency-based metric. This metric is +1 if the original and shifted orientation maps are the same, −1 if they are 90° apart and 0 if they are 45° apart or independent. In both regions, the autocorrelation functions of orientation and spatial frequency maps were similar (**Fig. 5e,j**). Both maps had a comparable rate of spatial decay, and they were both multimodal ('periodic') with a similar distance of ~800 μm (**Fig. 5e**, top) and ~600 μm (**Fig. 5e**, bottom) between peaks. Similar periodicities for

Figure 4 Bootstrap analysis to examine clustering of micro-maps. (**a**,**b**) Pairwise analysis for an example cell pairing in an orientation (**a**) and spatial frequency (**b**) map (~160 μm deep). Scale bar, 50 μm. This particular pairing with a distance of ~70 μm has an orientation and spatial frequency correlation (r_θ and r_ϕ) of 0.98 and −0.68 on the basis of the Gaussian fits shown above. (**c**) Functional clustering (*y* axis) relative to the distribution of the individual imaging regions. The clustering metric is based on the average correlation coefficient across pairings within a particular distance range (*x* axis), normalized by a resampled average. In this case the resampling was limited to cell pairs in the same imaging region. Each tick mark on the *x* axis is located at the mean distance between pairs for the given population of pairings. Significance above or below 1 (chance level) was computed from multiple trials of resampling. Both maps are significantly different than one for all distances ($P < 0.01$; bootstrap). (**d**) Functional clustering relative to our entire population of imaged neurons. Clustering was computed similarly to that in **c**, but resampling was between any two neurons of the entire data set. Clustering is significantly above 1 for all distances of both orientation and spatial frequency maps ($P < 0.01$; bootstrap).
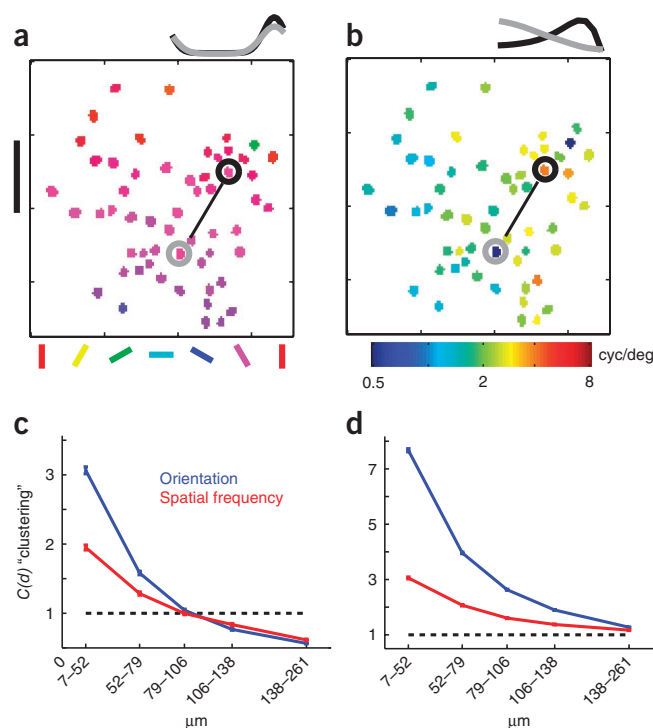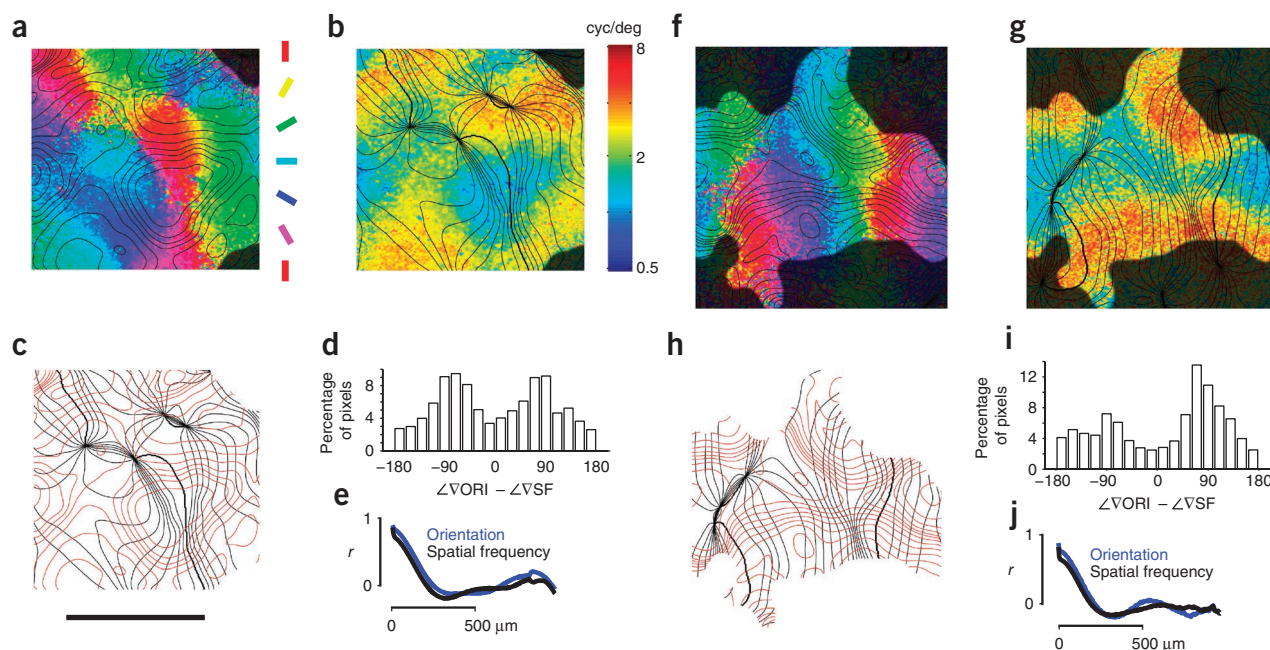
Figure 5 Relationship between orientation and spatial frequency maps. (**a**–**j**) Analysis for two cortical locations, each at an imaging depth of 260 μm (**a**–**e**) and 230 μm (**f**–**j**). (**a**,**f**) Orientation maps with the smoothed spatial frequency contours overlaid in black. (**b**,**g**) Corresponding spatial frequency maps with the smoothed orientation contours overlaid in black. (**c**,**h**) Combined orientation (black) and spatial frequency (red) contours. Scale bar, 0.5 mm. (**d**,**i**) Histograms showing the distribution of the intersection angle between orientation (ORI) and spatial frequency (SF) map gradients. The preferred intersections (94° and 84°) were computed from the histograms as the angle of a weighted sum of vectors. (**e**,**j**) Autocorrelation of both orientation (blue) and spatial frequency (black) maps, as a function of absolute cortical distance.

both spatial frequency and orientation are shown for three more imaging regions in **Supplementary Figure 2**.

In addition to quantifying the orthogonality between orientation and spatial frequency in the large-scale maps (**Fig. 5**), we tested whether a similar trend could be detected on the basis of the global gradient within our fine-scale imaging regions. This analysis required that we develop a metric that quantifies the axis of maximum change for each orientation and spatial frequency map by using the spatial layout of tuning curves at the discrete points of the cell bodies. To define this metric for the orientation map, we first defined a function that is its main dependency: $f_\theta(\lambda) = \text{median}[(1 - r_\theta)/d|\lambda]$. In this equation, r_θ is the correlation coefficient between the orientation tuning curve fits of two cells, d the distance between the cells and λ the angle of the line connecting the two cells (binned). In this and following equations, θ will denote orientation and ϕ will denote spatial frequency. To compute $f_\theta(\lambda)$, we divided all cell pairs into 10° bins on the basis of the angle of their connecting line and then computed $f_\theta(\lambda)$ as the median of $(1 - r_\theta)/d$ across all cell pairs within each bin centered at λ. The axis of maximum change for an orientation map (**Fig. 6a**) can now be defined as

$$A_\theta = \text{angle}\left(\sqrt{\sum_\lambda f_\theta(\lambda)e^{i2\lambda}}\right)$$

For spatial frequency maps (**Fig. 6b**), A_ϕ was defined by replacing r_θ with r_ϕ. Finally, the angle of intersection for each imaging region was computed as $90° - ||A_\theta - A_\phi| - 90°|$, which yields values near 0° for parallel gradients and values near 90° for perpendicular gradients. The distribution of these intersection angles clustered at 90° (**Fig. 6c**).

Fine-scale alignment of feature maps

We also analyzed the alignment of orientation and spatial frequency maps on a cell-by-cell basis, using the data obtained in the fine-scale imaging experiments. As in the measurements of map continuity (**Fig. 4**), the analysis is based on the tuning similarity between all cell pairs across all regions of interest, computed as the correlation coefficient between the tuning fits of orientation, r_θ, and spatial frequency, r_ϕ. We first binned the cell pairs into three cortical distances on the basis of the 33rd and 67th percentiles of the distance distribution. Within each distance bin, we generated a scatter plot where each
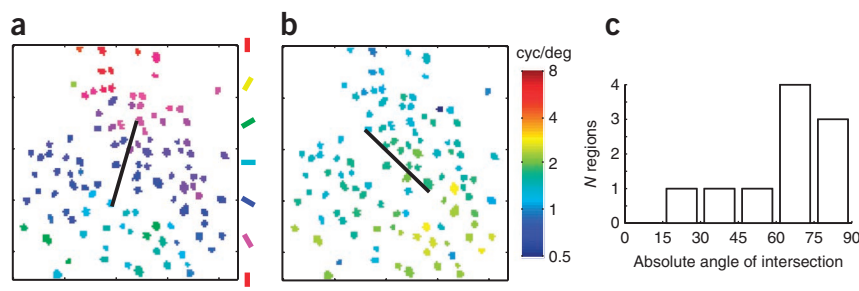

Figure 6 Measuring the angle of intersection between micro-maps of orientation and spatial frequency. The axis of maximum change was computed for each micro-map of orientation and spatial frequency, which then gave an axis of intersection for each imaged region. (**a**,**b**) An example orientation (**a**) and spatial frequency (**b**) map (160 μm deep), with the computed axes overlaid in black. The intersection for this region was ~60°. Scale bar, 50 μm. (**c**) A histogram of intersections from ten imaging regions.

Figure 7 Measuring orthogonality based on tuning curves of single neurons. (**a**–**c**) Joint distribution of pairwise orientation and spatial frequency tuning similarity. Similarly to the analysis for clustering in **Figure 4**, we computed the correlation coefficient between orientation (r_θ) and spatial frequency (r_ϕ) tuning curves for all cell pairs across nine imaging regions. Each cell pair was binned on the basis of the 33rd and 66th percentile of cortical distance of separation. The three images are the density plots for each of the distances. The dark intensity at each location represents the number of superimposed data points. The text in each inset gives the distance range for the subpopulation, along with the correlation coefficient and *P*-value of the scatter plot. For shorter distances (<72 μm), there is not a significant relationship between the maps. However, for the other two scatter plots (>72 μm), pairwise tuning similarity is negatively correlated between the orientation and spatial frequency maps. To better illustrate the trend, we have also plotted the mean of r_ϕ (blue) and r_θ (red), for each of three intervals on the opposing axis. Intervals were chosen to contain equal numbers of cell pairs. The s.e.m. bars are smaller than the width of the line.
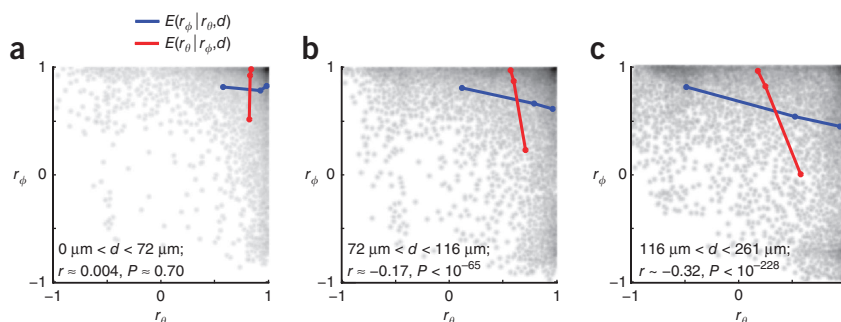
point compares r_θ and r_ϕ for the cell pair. These scatter plots were smoothed with a two-dimensional Gaussian (σ = 0.01) to create the density plots (**Fig. 7**). At the shortest cortical distance ($d < 72$ μm), the maps did not show a significant interdependence. This is most likely because they are dominated more by noise than by their gradients at this scale. However, with increasing cortical distance, the relationship became strongly anticorrelated as assessed by the Pearson correlation coefficient. This relationship shows that if a given pair of cells had the same tuning for orientation, they were likely to have different spatial frequency tuning, and vice versa, an observation that is consistent with the orthogonal contours determined in the large-scale imaging experiments.

For a more complete illustration of this trend in the density plots, we also computed the expected value of r_θ as a function of r_ϕ: $E(r_\theta|r_\phi)$. For this analysis, cell pairs in each scatter plot were divided into three bins on the basis of their r_ϕ value and the expected value of r_θ was computed across all the cell pairs in each bin. Bins were constructed such that they contained equal numbers of cell pairs. In a similar fashion, we also computed $E(r_\phi|r_\theta)$. This analysis confirmed that as r_ϕ increased, the expected value of r_θ decreased, and vice versa. This result was replicated by showing that the local variance of the orientation map is anticorrelated with the local variance of the spatial frequency map (**Supplementary Fig. 3c**).

DISCUSSION

We used two-photon Ca^{2+} imaging to study the microarchitecture of orientation and spatial frequency tuning in layer II/III of macaque monkey V1. Like orientation preference, spatial frequency preference had a notably smooth progression over the cortical surface. We quantified the cell-by-cell continuity of both orientation and spatial frequency tuning as a function of cortical distance in the horizontal dimension. Both maps showed significant continuity based on our bootstrap statistic; however, orientation maps were about twice as continuous as spatial frequency maps at the shortest distances. Using a similar metric, we also quantified the similarity of the maps at two depths separated by 100 μm. The similarity of the spatial frequency maps across depth was obvious, although statistically not as strong as the orientation map similarity for the same regions. Next we examined how the orientation and spatial frequency maps are jointly represented. We first captured the alignment of the map gradients determined in large-scale and fine-scale imaging experiments and showed that orientation and spatial frequency maps had orthogonal contours. Finally, we measured this relationship by means of the

pairwise comparisons of the tuning curves of individual cells. This showed that the maps had a systematically antagonistic relationship on a cell-by-cell basis.

Previous studies on spatial frequency maps

To our knowledge, this is the first study to show the precise layout and continuity of the spatial frequency map in Old World primates, as well as its alignment with the orientation map. Previous studies on the organization of spatial frequency tuning in these species are relatively sparse and have yielded inconsistent results. The first study to look for spatial frequency maps in macaques was based on 2DG uptake, which demonstrated that presentation of gratings with high or low spatial frequency resulted in a patchy activation pattern across V1 (ref. 19). However, this technique makes it difficult to quantify whether local transitions of spatial frequency preference exist. Subsequent single cell recordings lent support to clustering of spatial frequency preference, yet they came to different conclusions on the distribution and organization of spatial frequency tuning. Two studies reported gradual changes in spatial frequency preference along tangential recordings[16,18], whereas a third study found abrupt changes in spatial frequency preference[17]. It seems probable that a lacking consensus in the primate is simply a consequence of insufficient sampling density and spatial resolution in a map that is relatively noisy.

Several studies have looked at spatial frequency organization in other species, with most studies focusing on the cat. As in the monkey, the evidence regarding the layout of spatial frequency preference using electrophysiology and 2DG uptake is unsettled. Spatial frequency preference has been suggested to be organized in a laminar[25,26] or a columnar[27] fashion, or to lack consistency in either direction[28]. Recording from neighboring neurons in cat visual cortex, it was found that cell pairings share similar spatial frequency tuning preference, suggesting a clustered representation of spatial frequency in area 17 (ref. 29). However, another study using different stimuli but otherwise similar techniques did not find significant clustering of spatial frequency tuning[30]. Intrinsic signal imaging promised a more global and controlled analysis of spatial frequency organization. However, given that spatial frequency tuning is less clustered than orientation tuning as determined by electrophysiology[29], it is not surprising that the imaged spatial frequency maps are weaker and exhibit a less obvious structure than the orientation maps. Some authors propose that the spatial frequency maps are divided into regions of high and low spatial frequency preference[11,31], whereas others support a more continuous structure[12,32,33]. In terms of the alignment of spatial frequency

and orientation maps, a statistically significant relationship has been reported[11–13], yet it appears difficult to detect in most examples. Finally, the mere existence of spatial frequency maps in the cat has been called into question, largely on the basis largely of a reanalysis of data from these previous studies, with the claim that spatial frequency maps obtained with intrinsic imaging are an artifact of a nonspecific blood vessel–related response[14]. Perhaps the low signal-to-noise ratio in the spatial frequency maps acquired with intrinsic signal imaging is the root of the debate. In either case, the lack of regularity in spatial frequency organization requires that it be imaged at a cellular resolution for robust characterization.

Unique aspects of macaque monkey functional architecture

Many lines of functional and anatomical evidence indicate that V1 of macaque monkeys is quite different from cat area 17 (refs. 34–37). For example, even though both species have prominent orientation and ocular dominance columns, features related to spatial frequency encoding are different. Whereas both species have geniculate input channels carrying different ranges of spatial frequency (parvo- and magnocellular in the macaque versus X and Y in the cat), these are segregated at the input layer (layer IV) in macaques but not cats. Furthermore, local circuits distributing this information to more superficial layers are much more highly organized in the macaque and have tight relationships to cytochrome oxidase blobs. In macaque monkeys, the blobs receive a mixture of direct koniocellular input and both M and P input relayed through layers 4Cα and 4Cβ, respectively[36,37]. In contrast, interblobs receive less M input from 4Cα, which has been suggested as the basis for a somewhat higher prevalence of low spatial frequency tuned cells in blobs than interblobs[16]. While blobs also correspond to lower spatial frequency in cats[31], their blobs are less prominent than in macaques and it has been suggested that their low spatial frequency preferences arise from a stronger, direct Y-cell input[31,38] rather than differences in local connectivity.

In view of the differences in circuit organization that might mediate a functional architecture for spatial frequency encoding in cats versus monkeys, it should not be surprising that the strength and regularity of any relationships between spatial frequency and other functional maps might also be different. The organization between orientation and spatial frequency maps reported from intrinsic imaging studies in cats is one of a 'loose orthogonality' whereby other feature maps can also be squeezed into the architecture without sacrificing too much coverage[39]. A similar result was also shown in the ferret[13]. In contrast, we have observed a much sharper and regular association between orientation and spatial frequency maps in the macaque monkey. It remains to be determined whether this relationship would appear stronger in cats or ferrets if the more sensitive two-photon imaging methods are used, but it is likely that the tight relationship between orientation and spatial frequency maps observed here does not exist in the other species studied. This is the case for other cortical maps. For example, there is a pronounced species-dependent difference in the alignment between cytochrome oxidase blobs and ocular dominance bands. In the macaque (and human), blobs tightly align with ocular dominance columns, yet this relationship is nonexistent in squirrel monkeys and appears weak at best in the cat[5]. In addition, the relationship between orientation and ocular dominance is stronger in the monkey[7,8] than in the ferret[13,40,41] and perhaps the cat as well[11]. The tight orientation–spatial frequency and orientation–ocular dominance relationships in the monkey combine to suggest a parallel alignment of spatial frequency and ocular dominance maps, which is in stark contrast to what has been shown using intrinsic imaging in other species. Such a relationship between spatial frequency and ocular dominance maps is also consistent with the alignment between blobs and ocular dominance and the (likely) alignment between blobs and spatial frequency maps. Also, parallel spatial frequency and ocular dominance gradients do not necessarily imply a lack of spatial frequency coverage for each eye, as the spatial period of the ocular dominance map would be twice that of the spatial frequency map. More specifically, it suggests that the most monocular regions tend to have lower spatial frequency preference.

Concluding remarks

The importance of characterizing V1 functional maps is twofold: to better understand how map continuity may benefit wiring efficiency yet restrict coverage[42,43] and to constrain network models on the development and mechanisms of neuronal tuning in visual cortex[44–48]. These research avenues will benefit from the information provided by two-photon imaging, as they will ultimately require knowledge of the cell-by-cell distribution of tuning shape within the cortical space. The systematic relationship between orientation and spatial frequency tuning we have demonstrated here, along with other recent results on the exquisite layout of tuning in highly visual mammals[22,49,50], are crucial steps toward establishing a complete picture of cortical feature maps in V1.

METHODS

Methods and any associated references are available in the online version of the paper.

Note: Supplementary information is available in the online version of the paper.

AUTHOR CONTRIBUTIONS
I.N., K.J.N. and E.M.C. designed the research. I.N., K.J.N., A.A.D. and E.M.C. performed experiments. I.N. analyzed the data. I.N., K.J.N. and E.M.C. wrote the paper.

COMPETING FINANCIAL INTERESTS
The authors declare no competing financial interests.

1. Hubel, D.H. & Wiesel, T.N. Receptive fields, binocular interaction and functional architecture in the cat's visual cortex. *J. Physiol. (Lond.)* **160**, 106–154 (1962).
2. Hubel, D.H. & Wiesel, T.N. Receptive fields and functional architecture of monkey striate cortex. *J. Physiol. (Lond.)* **195**, 215–243 (1968).
3. Blasdel, G.G. & Salama, G. Voltage-sensitive dyes reveal a modular organization in monkey striate cortex. *Nature* **321**, 579–585 (1986).
4. Ts'o, D.Y., Frostig, R., Lieke, E. & Grinvald, A. Functional organization of primate visual cortex revealed by high resolution optical imaging. *Science* **249**, 417–420 (1990).
5. Horton, J.C. & Adams, D.L. The cortical column: a structure without a function. *Phil. Trans. R. Soc. Lond. B* **360**, 837–862 (2005).
6. Hubel, D.H. & Wiesel, T.N. Functional architecture of macaque monkey visual cortex (Ferrier Lecture). *Proc. R. Soc. Lond. B Biol. Sci.* **198**, 1–59 (1977).
7. Obermayer, K. & Blasdel, G.G. Geometry of orientation and ocular dominance columns in monkey striate cortex. *J. Neurosci.* **13**, 4114–4129 (1993).
8. Bartfeld, E. & Grinvald, A. Relationships between orientation-preference pinwheels, cytochrome oxidase blobs, and ocular-dominance columns in primate striate cortex. *Proc. Natl. Acad. Sci. USA* **89**, 11905–11909 (1992).
9. Crair, M.C., Ruthazer, E.S., Gillespie, D.C. & Stryker, M.P. Ocular dominance peaks at pinwheel center singularities of the orientation map in cat visual cortex. *J. Neurophysiol.* **77**, 3381–3385 (1997).
10. Blasdel, G. & Campbell, D. Functional retinotopy of monkey visual cortex. *J. Neurosci.* **21**, 8286–8301 (2001).

11. Hübener, M., Shoham, D., Grinvald, A. & Bonhoeffer, T. Spatial relationships among three columnar systems in cat area 17. *J. Neurosci.* **17**, 9270–9284 (1997).

12. Issa, N.P., Trepel, C. & Stryker, M.P. Spatial frequency maps in cat visual cortex. *J. Neurosci.* **20**, 8504–8514 (2000).

13. Yu, H., Farley, B.J., Jin, D.Z. & Sur, M. The coordinated mapping of visual space and response features in visual cortex. *Neuron* **47**, 267–280 (2005).

14. Sirovich, L. & Uglesich, R. The organization of orientation and spatial frequency in primary visual cortex. *Proc. Natl. Acad. Sci. USA* **101**, 16941–16946 (2004).

15. Kim, D.S., Matsuda, Y., Ohki, K., Ajima, A. & Tanaka, S. Geometrical and topological relationships between multiple functional maps in cat primary visual cortex. *Neuroreport* **10**, 2515–2522 (1999).

16. Edwards, D.P., Purpura, K.P. & Kaplan, E. Contrast sensitivity and spatial frequency response of primate cortical neurons in and around the cytochrome oxidase blobs. *Vision Res.* **35**, 1501–1523 (1995).

17. Born, R.T. & Tootell, R.B. Spatial frequency tuning of single units in macaque supragranular striate cortex. *Proc. Natl. Acad. Sci. USA* **88**, 7066–7070 (1991).

18. Silverman, M.S., Grosof, D.H., De Valois, R.L. & Elfar, S.D. Spatial-frequency organization in primate striate cortex. *Proc. Natl. Acad. Sci. USA* **86**, 711–715 (1989).

19. Tootell, R.B., Silverman, M.S., Hamilton, S.L., Switkes, E. & De Valois, R.L. Functional anatomy of macaque striate cortex. V. Spatial frequency. *J. Neurosci.* **8**, 1610–1624 (1988).

20. Horton, J.C. Cytochrome oxidase patches: a new cytoarchitectonic feature of monkey visual cortex. *Phil. Trans. R. Soc. Lond. B* **304**, 199–253 (1984).

21. Stosiek, C., Garaschuk, O., Holthoff, K. & Konnerth, A. In vivo two-photon calcium imaging of neuronal networks. *Proc. Natl. Acad. Sci. USA* **100**, 7319–7324 (2003).

22. Ohki, K. *et al.* Highly ordered arrangement of single neurons in orientation pinwheels. *Nature* **442**, 925–928 (2006).

23. Ringach, D.L., Sapiro, G. & Shapley, R. A subspace reverse-correlation technique for the study of visual neurons. *Vision Res.* **37**, 2455–2464 (1997).

24. Nauhaus, I., Nielsen, K.J. & Callaway, E.M. Nonlinearity of two-photon Ca^{2+} imaging yields distorted measurements of tuning for V1 neuronal populations. *J. Neurophysiol.* **107**, 923–936 (2012).

25. Maffei, L. & Fiorentini, A. Spatial frequency rows in the striate visual cortex. *Vision Res.* **17**, 257–264 (1977).

26. Berardi, N., Bisti, S., Cattaneo, A., Fiorentini, A. & Maffei, L. Correlation between the preferred orientation and spatial frequency of neurones in visual areas 17 and 18 of the cat. *J. Physiol. (Lond.)* **323**, 603–618 (1982).

27. Tootell, R.B., Silverman, M.S. & De Valois, R.L. Spatial frequency columns in primary visual cortex. *Science* **214**, 813–815 (1981).

28. Tolhurst, D.J. & Thompson, I. Organization of neurones preferring similar spatial frequencies in cat striate cortex. *Exp. Brain Res.* **48**, 217–227 (1982).

29. DeAngelis, G.C., Ghose, G.M., Ohzawa, I. & Freeman, R.D. Functional micro-organization of primary visual cortex: receptive field analysis of nearby neurons. *J. Neurosci.* **19**, 4046–4064 (1999).

30. Molotchnikoff, S., Gillet, P.-C., Shumikhina, S. & Bouchard, M. Spatial frequency characteristics of nearby neurons in cats' visual cortex. *Neurosci. Lett.* **418**, 242–247 (2007).

31. Shoham, D., Huebener, M., Schulze, S., Grinvald, A. & Bonhoeffer, T. Spatio-temporal frequency domains and their relation to cytochrome oxidase staining in cat visual cortex. *Nature* **385**, 529–33 (1997).

32. Everson, R.M. *et al.* Representation of spatial frequency and orientation in the visual cortex. *Proc. Natl. Acad. Sci. USA* **95**, 8334–8338 (1998).

33. Xu, X., Anderson, T.J. & Casagrande, V.A. How do functional maps in primary visual cortex vary with eccentricity? *J. Comp. Neurol.* **501**, 741–755 (2007).

34. Gilbert, C.D. Microcircuitry of the visual cortex. *Annu. Rev. Neurosci.* **6**, 217–247 (1983).

35. Martin, K.A.C. Neuronal circuits in cat striate cortex. in *Cerebral Cortex* (eds. Jones, E.G. & Peters, A.) 2:241–2:284 (Plenum, New York, 1984).

36. Callaway, E.M. Local circuits in primary visual cortex of the macaque monkey. *Annu. Rev. Neurosci.* **21**, 47–74 (1998).

37. Nassi, J.J. & Callaway, E.M. Parallel processing strategies of the primate visual system. *Nat. Rev. Neurosci.* **10**, 360–372 (2009).

38. Boyd, J.D. & Matsubara, J.A. Laminar and columnar patterns of geniculocortical projections in the cat: relationship to cytochrome oxidase. *J. Comp. Neurol.* **365**, 659–682 (1996).

39. Swindale, N.V., Shoham, D., Grinvald, A., Bonhoeffer, T. & Hübener, M. Visual cortex maps are optimized for uniform coverage. *Nat. Neurosci.* **3**, 822–826 (2000).

40. Issa, N.P., Trachtenberg, J.T., Chapman, B., Zahs, K.R. & Stryker, M.P. The critical period for ocular dominance plasticity in the ferret's visual cortex. *J. Neurosci.* **19**, 6965–6978 (1999).

41. White, L.E., Bosking, W. & Fitzpatrick, D. Consistent mapping of orientation preference across irregular functional domains in ferret visual cortex. *Vis. Neurosci.* **18**, 65–76 (2001).

42. Durbin, R. & Mitchison, G. A dimension reduction framework for understanding cortical maps. *Nature* **343**, 644–647 (1990).

43. Koulakov, A.A. & Chklovskii, D. Orientation preference patterns in mammalian visual cortex: a wire length minimization approach. *Neuron* **29**, 519–527 (2001).

44. Swindale, N.V. The development of topography in the visual cortex: a review of models. *Network* **7**, 161–247 (1996).

45. Ferster, D. & Miller, K. Neural mechanisms of orientation selectivity in the visual cortex. *Annu. Rev. Neurosci.* **23**, 441–471 (2000).

46. McLaughlin, D., Shapley, R. & Shelley, M. Large-scale modeling of the primary visual cortex: influence of cortical architecture upon neuronal response. *J. Physiol. Paris* **97**, 237–252 (2003).

47. Paik, S.-B. & Ringach, D.L. Retinal origin of orientation maps in visual cortex. *Nat. Neurosci.* **14**, 919–925 (2011).

48. Kaschube, M. *et al.* Universality in the evolution of orientation columns in the visual cortex. *Science* **330**, 1113–1116 (2010).

49. Li, Y., Van Hooser, S.D., Mazurek, M., White, L.E. & Fitzpatrick, D. Experience with moving visual stimuli drives the early development of cortical direction selectivity. *Nature* **456**, 952–956 (2008).

50. Kara, P. & Boyd, J.D. A micro-architecture for binocular disparity and ocular dominance in visual cortex. *Nature* **458**, 627–631 (2009).

ONLINE METHODS

Animal preparation and surgery. All procedures were conducted in accordance with guidelines of the US National Institutes of Health and were approved by the Institutional Animal Care and Use Committee at the Salk Institute. We used five juvenile macaque monkeys (four *Macaca fascicularis*, one *M. radiata*; ages 9–18 months). Animals were anesthetized with ketamine (10 mg/kg, i.m.) and pretreated with atropine (0.04 mg/kg, i.m.). They were placed in a stereotaxic apparatus, in which initially the animal's head was rigidly held in the stereotaxic frame by ear bars, eye bars and a palate clamp (David Kopf Instruments). Anesthesia was maintained throughout the experiment with sufentanil citrate (4–20 μg kg^{-1} h^{-1}, i.v.), supplemented with isoflurane (0.5–2%) during surgeries. We additionally administered diazepam (50–100 μg/kg, i.v.) as needed. For one animal, we supplemented sufentanil anesthesia with low levels of isoflurane (around 0.5%) throughout the entire experiment. Animals were paralyzed using pancuronium bromide (0.1–0.2 mg kg^{-1} h^{-1}, i.v.) and artificially ventilated using a small animal respirator (Harvard Apparatus or Ugo Basile). The EKG, EEG, SpO$_2$, heart rate and body temperature were monitored continuously to judge the animal's health and maintain proper anesthesia. Dexamethasone (0.1 mg/kg, i.m.) and cefazolin (25 mg/kg, i.v.) were administered every 24 h to reduce brain swelling and prevent infections.

We then attached a small metal post (about 1×2 cm) to the skull over frontal cortex using metal screws and dental cement (Grip Cement, Dentsply). For the rest of the experiment, we used this head post to hold the animal's head by connecting it to the stereotaxic apparatus. At this point, ear bars and eye bars were removed, but the palate clamp remained in place. Securing the animal's head by both head post and palate clamp helped to reduce the amount of breathing-induced motion artifacts during imaging.

The skull over the occipital lobe was thinned, and a custom-made imaging well was attached over V1 (see **Supplementary Fig. 4**). Within the well perimeter, we made small craniotomies and durotomies (about 3×3 mm) to expose the brain. Dye was then injected as described in ref. 24. Briefly, we injected a solution containing 2 mM OGB and 25% SR101 in ACSF[21,51]. After dye injection, the exposed brain was covered with agarose (1.5% in ACSF; type III-A, Sigma-Aldrich) and a coverslip (World Precision Instruments). To further reduce motion artifacts, the coverslip was gently pushed down by clamps attached to the imaging well. This was sufficient to remove most vertical movement. However, there was usually an appreciable amount of residual horizontal movement, which was corrected offline using an optical flow–based method (**Supplementary Fig. 5**). After successful dye injections, we could often image neurons down to ~400 μm; however our data was most often collected at depths between ~140 μm and ~300 μm. After collecting sufficient data from each imaging region, or when the dye loading failed to produce well-labeled neurons, we performed a new craniotomy and durotomy and repeated the dye loading in the new location. Usually, we were able to perform about five craniotomies/durotomies without having to move the imaging well. Whenever we could fit no more craniotomies within the imaging well, it was moved to a new position on the skull.

Eyes were dilated with 1% atropine and corneas protected with contact lenses. Refraction of the eyes was determined for two monitor distances (60 and 80 cm). In initial experiments, we used neural responses recorded on metal electrodes to determine the ophthalmic lenses yielding the 'best' spatial frequency tuning curves. For later experiments, we instead used responses from two-photon imaging.

Two-photon microscope setup. We used the same two-photon microscope as described in ref. 24 and fixed the excitation wavelength at 920 nm. Large-scale imaging was performed using a 16×, 0.8 NA objective (Nikon); fine-scale imaging experiments used a 40×, 0.8 NA lens (Olympus). Technical limitations of the microscope kept us from overfilling the back aperture of the 16× objective, which reduces the effective NA. The beam size was large enough to overfill the back aperture of the 40× objective. For drifting grating experiments, images were acquired at a frame rate between 2 and 8 Hz. For flashed grating experiments, the frame rate was 16 Hz. ScanImage software was used for data acquisition (ref. 52).

Visual stimuli. Visual stimuli were generated using the Psychophysics Toolbox extensions for Matlab[53,54] on a 17-inch CRT monitor (1024×768) with a refresh rate of 100 Hz. The monitor was gamma corrected using a Photo Research-701 spectroradiometer. We ran a set of three preliminary stimuli to help optimize the spatial frequencies and retinotopic location of the stimulus for each imaging

region. The first was a large (~$60° \times 60°$) drifting square-wave grating stimulus at eight orientations, which gave the preferred orientations within the ROI. In the next experiment, we presented sine-wave drifting gratings at five spatial frequencies (0.5, 1.0, 2.0, 4.0 and 8.0 cyc/deg), each at one or two directions. Finally, we ran a retinotopy stimulus as described in ref. 24. In subsequent experiments the size of the stimulus was then kept between 5° and 6°.

In fine-scale imaging experiments, we showed a random grating noise stimulus to one eye. Each presentation randomly pooled from a set of gratings of different orientation, spatial frequency and spatial phase. The stimulus set varied across experiments, but there were always four phases for each orientation and spatial frequency. The domain of orientations and spatial frequencies were organized into Cartesian coordinates. Spatial frequency was spaced either linearly or logarithmically, with the range defined by the preliminary experiments. Depending on the experiment, the stimulus was updated every 150 or 200 ms and each trial lasted 60 s. Gratings were shown at full contrast, and a gray screen was shown instead of a grating 5% of the time.

For large-scale imaging, we presented drifting gratings because responses are more sustained and can thus be captured with a slower scan rate, which was required to image at an acceptable resolution. Furthermore, drifting gratings were deemed adequate since we were computing the preferred orientation/spatial frequency at each pixel and less concerned about distortion of the tuning curve[24]. Drifting gratings were shown to one eye at 8 directions (45° steps) and 5 spatial frequencies (0.5 to 8 cyc/deg). All combinations of direction and spatial frequency were randomly interleaved and shown 6 to 7 times.

Computing the tuning curves. *Large-scale imaging.* The response time course of each pixel for each trial was first computed as $(F(t) - F_o)/F_o$, where F_o is the mean response to the gray screen before stimulus onset for the given trial. Next, each frame of the trial was smoothed with a narrow two-dimensional Gaussian ($\sigma = 1.5$ μm). We then computed the average and standard error response time course to each stimulus at each pixel (**Fig. 1a–d**). Responses were averaged across all presentations of the same stimulus and the time window from 0.2 to 3.0 s after stimulus onset. To compute the orientation and spatial frequency tuning curves at each pixel, we averaged over spatial frequency and orientation, respectively. Orientation preference was measured as the direction of the resultant of response vectors. Spatial frequency preference was measured as the tuning curve's center-of-mass, after taking the log of the domain. For further analysis, the imaging region was cropped based on a signal-to-noise ratio (SNR) metric. We first computed the SNR at the time-to-peak of the best stimulus, at each pixel. SNR was measured as $(\mu_{max} - \mu_{min})/(\text{SE}_{max} + \text{SE}_{min})$, where μ_{max} and μ_{min} are the mean responses to the best and worst stimulus, and SE_{max} and SE_{min} are the corresponding standard errors. Next, this 'SNR image' was smoothed with a two-dimensional Gaussian ($\sigma = 25$ μm). The cropped ROI used for analyses (**Figs. 2** and **5**) consisted of pixels with SNR > 2.

Fine-scale imaging. For each imaging region, we created a binary cell mask for each cell body to define the overlapping set of pixels[24]. To account for glia selectively labeled with SR101, cells were removed that were present in both the red (575 to 650 nm emission filter) and green (510 to 560 nm emission filter) channel. To compute the response of a neuron at each frame, we took the dot product between a Gaussian-smoothed ($\sigma = 1$ μm) binary cell mask and the raw image. Movement correction was implemented by shifting the location of the Gaussian before smoothing the mask (**Supplementary Fig. 6**). **Supplementary Video 1** shows one trial, with the movement correction depicted for two neurons. See **Supplementary Figures 7** and **8** for a comparison of responses at the cell body to those at the adjacent neuropil.

Prior to computing the kernels for the flashed gratings, we convolved the signal for each neuron with a difference-of-Gaussians function ($\sigma_{lowpass} = 50$ ms; $\sigma_{highpass} = 5,000$ ms) to help remove noise. Responses from each neuron were then Z-scored within each 60 s trial. Next, we computed the mean and standard error of the fluorescence response (in Z units) to each type of grating in the ensemble, followed by subtracting the blank response from each time course. That is, the spatiotemporal kernel is defined as $K(\mathbf{p},\tau) = E[R|\mathbf{p},\tau] - E[R|b,\tau]$. $E[R|\mathbf{p},\tau]$ is the expected response (R) given a set of stimulus parameters ($\mathbf{p}$) and time after stimulus onset (τ). $E[R|b,\tau]$ is the expected response given that a 'blank' was presented. Orientation tuning curves were then computed from $K(\mathbf{p},\tau)$ as follows: (i) we averaged over spatial phase, (ii) took the slice at the time delay of maximum response, and finally (iii) took a weighted sum over spatial frequency,

where the weighting function is simply the mean of the kernel over orientation. Spatial frequency tuning curves were computed in the equivalent manner, such that the weighting function in orientation is the average over spatial frequency.

The first criterion for data selection was based on whether cells responded to the optimal stimulus reliably higher than to the worst stimulus. We included cells that had $(\mu_{max} - \mu_{min})/(\text{SE}_{max} + \text{SE}_{min}) > 1$. Here, $\mu_{max} = E[R|\mathbf{p}_{max}, \tau_{peak}]$, $\mu_{min} = E[R|\mathbf{p}_{min}, \tau_{peak}]$, and SE_{max} and SE_{min} are the corresponding standard errors. Approximately 94% of neurons passed this criterion. The second criterion was based on the quality of the fits to the orientation and spatial frequency tuning curves. Orientation tuning curves were fit by a Gaussian and spatial frequency tuning curves by a difference-of-Gaussians. We only included cells for which both fits accounted for at least 60% of the variance, which was 93% of the cells that passed the SNR criterion. This second criterion was implemented to ensure the accuracy of our pairwise tuning similarity measurements, as they are based on the correlation coefficient between these fits.

Quantifying map similarity across depth. Orientation and spatial frequency maps were obtained at multiple depths with large-scale imaging (**Fig. 2**). To quantify the degree of consistency that each feature map maintains across two imaging planes separated by 100 μm in layer II/III, we computed the following statistics:

$$\text{Depth consistency}_{orientation} = E[|\Delta\theta|_{resampled}]/E[|\Delta\theta|_{actual}] \qquad (1)$$

$$\text{Depth consistency}_{spatial\ frequency} = E[|\Delta\phi|_{resampled}]/E[|\Delta\phi|_{actual}] \qquad (2)$$

The denominators are the pixel-by-pixel absolute difference between the images at the two depths ($|\Delta\theta| = |\theta_{depth1} - \theta_{depth2}|$; mod 180) and spatial frequencies ($|\Delta\phi| = |\log_2(\phi_{depth1}/\phi_{depth2})|$), then averaged over pixels. The numerator is the average $|\Delta\theta|$ or $|\Delta\phi|$ from randomly sampled pixel locations at each depth (with replacement). The number of samples for each resampling trial equaled the number of pixels. If equation (1) value was greater than equation (2) value for more than 99% of trials, then the corresponding map was deemed significantly more consistent across depth.

Characterizing functional map continuity. We compared the functional clustering between orientation and spatial frequency maps using a normalized measure of the average tuning difference between pairs of neurons (**Fig. 4**). Specifically, clustering is defined as

$$\text{Clustering}(d) = E[1 - r_{resampled}]/E[1 - r_{actual}|d] \qquad (3)$$

where d denotes the distance between cells, r is the correlation coefficient between the tuning curve fits (either orientation or spatial frequency, defined 'r_θ' and 'r_ϕ') of a cell pair and E is the expected value. Thus, the denominator is the average 'tuning dissimilarity' between a pair of cells separated by a particular distance. The numerator is the average tuning dissimilarity between a randomly selected pair of cells. We created the pool of randomly selected cell pairs in two ways. First, the pool was created by resampling (with replacement) cell pairs contained in the same imaging region (**Fig. 4c**). For each resampling trial, the number of samples

from each imaging region equaled the actual number of cell pair combinations in that region. So the total number of samples for each trial equaled

$$\sum_R \frac{n_R!}{2(n_R - 2)!}$$

where n_R is the number of cells in imaging region R. Second, we instead created the random pool by taking any two cell pairs (with replacement) in the entire data set of ten imaging regions (**Fig. 4d**). The number of selected pairs for each trial was the same as above. For each method of resampling, there were 1,000 resampling trials. If Clustering(d) was either >1 or <1 for at least 99% of the resampling trials, then we concluded that the map showed significant structure at the given distance.

Characterizing the joint representation of orientation and spatial frequency.
Large-scale imaging. Orientation and spatial frequency maps were smoothed before computing their contours and gradients (**Fig. 5**). To smooth the orientation map, we first converted it into a complex valued image. Specifically, $\theta(x,y)$ was converted to $\exp(i2\theta(x,y))$. The smoothed complex image was then converted back to orientation by taking the angle/2. For both orientation and spatial frequency maps, the smoothing operator was a two-dimensional Gaussian with $\sigma = 25$ μm. The gradient of the smoothed orientation and spatial frequency maps were computed at each pixel, based on the tuning differences between pixels computed as described for the variables in eqs. 1 and 2. That is, we computed $\Delta\theta$ and $\Delta\phi$ in the x and y dimensions to create real and imaginary components of complex-valued matrices. The difference in phase of the gradients was then computed as described in the Results section.

Fine-scale imaging. We binned cell pairs into three bins according to their cortical distance, using the 33rd and 67th percentile as the boundaries for the bins (**Fig. 7**). Within each distance bin, we quantified the joint distribution of r_θ and r_ϕ either by computing the Pearson correlation coefficient between the two values, or by computing mean and standard error for r_θ as a function of r_ϕ or vice versa.

Autocorrelation of maps. For the large-scale maps, we computed the autocorrelation as a function of absolute cortical distance, $R(d)$ (**Fig. 5**). For spatial frequency maps, R was computed as the correlation coefficient between the log of the maps for a given shift, d. For orientation maps we could not use the Pearson correlation coefficient, as it is a circular variable. Instead, R was computed based on the projection of the coherency between the maps for each shift. Specifically, we first compute the coherency, $\text{Coh}(d) = E[\exp(-i2\theta_d)\exp(i2\theta)]$, which is the mean of the pixel-by-pixel product between two complex images that are a function of the orientation map, θ, given that one has been shifted by d. We then take $R_\theta(d) = |\text{Coh}(d)| \times \cos[\text{angle}(\text{Coh}(d))]$ as the 'correlation coefficient' for the orientation maps. This metric will be 1 if θ and θ_d are the same, −1 if they are 90° apart, and ~0 if they are 45° apart or independent. For both orientation and spatial frequency autocorrelation functions, we only take into account the pixels that overlap within the SNR defined imaging region (see above) for each shift. Thus, larger shifts use fewer pixels to compute R.

51. Nimmerjahn, A., Kirchhoff, F., Kerr, J.N.D. & Helmchen, F. Sulforhodamine 101 as a specific marker of astroglia in the neocortex *in vivo*. *Nat. Methods* **1**, 31–37 (2004).
52. Pologruto, T.A., Sabatini, B.L. & Svoboda, K. ScanImage: flexible software for operating laser scanning microscopes. *Biomed. Eng. Online* **2**, 13 (2003).
53. Brainard, D.H. The psychophysics toolbox. *Spat. Vis.* **10**, 433–436 (1997).
54. Pelli, D.G. The VideoToolbox software for visual psychophysics: transforming numbers to movies. *Spat. Vis.* **10**, 437–442 (1997).

Erratum: Orthogonal micro-organization of orientation and spatial frequency in primate primary visual cortex

Ian Nauhaus, Kristina J Nielsen, Anita A Disney & Edward M Callaway

In the version of this article initially published, the scale bar length for Figure 1e was misstated as 500 μm. The correct length is 50 μm. The error has been corrected in the HTML and PDF versions of the article.

Corrigendum: Orthogonal micro-organization of orientation and spatial frequency in primate primary visual cortex

In the version of this article initially published, the computation performed to yield the values on the *x* axis of Figure 6c was incorrectly defined in the text and on the axis label as the absolute difference between A_θ and A_ϕ (mod 90°). The correct computation is $90° - \left| \left| A_\theta - A_\phi \right| - 90° \right|$, which yields values near 0° for parallel gradients and values near 90° for perpendicular gradients. The error has been corrected in the HTML and PDF versions of the article.

Erratum: Orthogonal micro-organization of orientation and spatial frequency in primate primary visual cortex

Ian Nauhaus, Kristina J Nielsen, Anita A Disney & Edward M Callaway

In the version of this article initially published, in the equation for A_θ on p. 5, the subscript to the variable f was given as an e. The correct character is θ. The error has been corrected in the HTML and PDF versions of the article.